Check for updates

Journal of Pathology
J Pathol 2026
Published online 00 Month 0000 in Wiley Online Library
(wileyonlinelibrary.com) DOI: 10.1002/path.70033

ORIGINAL ARTICLE

Extracellular matrix remodeling as a unique mechanism of expansion of periprostatic adipose tissue: implication for prostate cancer aggressiveness

David Estève[1], Aurélie Toulet[1], Mathieu Roumiguié[1,2], Dawei Bu[3], Mathilde Lacombe[1], Sarah Péricart[4], Chloé Belles[5], Cécile Manceau[1,2], Cynthia Houël[1], Manuelle Ducoux-Petit[1,6], Nathalie Van Acker[4], Stéphanie Dauvillier[1], Yiyue Jia[1], Marine Hernandez[1], Mohammed Moutahir[1], Camille Franchet[4], Nicolas Doumerc[2], Mathieu Thoulouzan[2], Sophie Le Gonidec[7], Philippe Valet[7], Bernard Malavaud[2], Odile Burlet-Schiltz[1,6], Anne Bouloumié[5], Philipp E Scherer[3], Delphine Milhas[1]* and Catherine Muller[1]*

[1] *Institut de Pharmacologie et de Biologie Structurale (IPBS), Université de Toulouse, CNRS (Équipe Labélisée Ligue Nationale contre le Cancer), Toulouse, France*
[2] *Department of Urology and Renal Transplantation, Toulouse University Hospital, Institut Universitaire du Cancer de Toulouse, Toulouse, France*
[3] *Touchstone Diabetes Center, Department of Internal Medicine and Department of Cell Biology, University of Texas Southwestern Medical Center, Dallas, TX, USA*
[4] *Department of Pathology, Institut Universitaire du Cancer de Toulouse, Toulouse, France*
[5] *Institut des Maladies Métaboliques et Cardiovasculaires, Université de Toulouse, INSERM, Toulouse, France*
[6] *Infrastructure Nationale de Protéomique, ProFI, Toulouse, France*
[7] *Institut RESTORE, Université de Toulouse, CNRS U-5070, EFS, ENVT, INSERM U1301, Toulouse, France*

*Correspondence to: C Muller, IPBS CNRS UMR 5089, 205 route de Narbonne, 31077 Toulouse, France. E-mail: muller@ipbs.fr; D Milhas, IPBS CNRS UMR 5089, 205 route de Narbonne, 31077 Toulouse, France. E-mail: milhas@ipbs.fr

Abstract

One of the most striking features of the adipose depot surrounding the prostate [periprostatic adipose tissue (PPAT)] is that its accumulation is independent of body mass index. Its volume varies considerably between individuals, with some patients exhibiting abundant PPATs, which have been correlated to the occurrence of aggressive prostate cancer (PCa). However, abundant PPAT is not well defined at the biological level. We used a new statistical approach to define abundant PPAT by normalizing PPAT volume to prostate volume in a cohort of 351 patients using a linear regression model. Applying this definition, we confirmed the link between abundant PPAT and PCa aggressiveness, thereby validating our approach. At the biological level, we showed that abundant PPAT exhibited extensive extracellular matrix remodeling, notably of the collagen network, decreasing the mechanical constraints in hypertrophic adipocytes, leading to inflammation-free expansion. Degradation of the most abundant collagen in adipose tissue (AT), collagen VI, was associated with increased production of endotrophin, a signaling peptide derived from AT that was also elevated in the urine of patients with abundant PPAT confirming the clinical relevance of our results. These results highlight a unique mechanism of expansion of an adipose depot and open new mechanistic avenues to explain its role in prostate-related disorders.
© 2026 The Pathological Society of Great Britain and Ireland.

Keywords: periprostatic adipose tissue; prostate cancer; adipocyte hypertrophy; extracellular matrix; collagen VI; endotrophin (ETP); inflammation

Received 13 June 2025; Revised 6 November 2025; Accepted 31 December 2025

No conflicts of interest were declared.

Introduction

Periprostatic adipose tissue (PPAT) is a white adipose tissue (WAT) that surrounds the prostate. Although it shares common vasculature with the prostate, it is separated from it by a fibromuscular sheet called the prostate capsule. Nevertheless, one-third of the anterior zone of the prostate is in direct contact with this tissue [1]. Like other WAT, PPAT consists mainly of adipocytes and other cell types in the stromal vascular fraction (SVF), including adipose progenitor cells, fibroblasts, endothelial cells, and immune cells, all of which are embedded in the extracellular matrix (ECM) [2,3]. Also, as a WAT, PPAT is an active metabolic and secretory organ [4]. Accordingly, PPAT can impact various prostate-related diseases, including benign prostate hyperplasia (BPH), erectile and urethral dysfunctions, and prostate cancer (PCa), although its physiological roles remain mainly uncharacterized [5–7].

One of the most striking features of PPAT is that its accumulation is independent of body mass index (BMI), which is, to our knowledge, a unique feature among adipose depots [6,8]. By comparison with abdominal

© 2026 The Pathological Society of Great Britain and Ireland. www.pathsoc.org

pelvic adipose tissue, which behaves like a typical WAT, we found that PPAT (in both healthy and cancer-bearing patients) had a sparse vascular network responsible for a chronic hypoxic state leading to a dense collagen network typical of fibrosis in lean patients [8]. In opposition to the control AT, no increase in this collagen network was observed in PPAT between lean individuals and individuals with obesity [8]. We proposed that this obesity-like organization of the ECM in PPAT does not adapt to external signals but provides an important physical constraint on PPAT expansion [8]. A recent study demonstrated that obesity was not associated with adipocyte hypertrophy in PPAT [9], consistent with the idea that PPAT is in a state of maximum expandability in most individuals.

However, the volume of PPAT varies considerably between patients, highlighting that PPAT has the capacity to expand upon uncharacterized mechanisms [8,10,11]. Recent clinical studies demonstrated that patients with large amounts of PPAT had more aggressive PCa [6]. PPAT abundance correlates with prostate tumors with high Gleason scores and local and distant dissemination [6,10–16]. Taken together, these studies suggest that the expansion of PPAT may be far more important than obesity in determining the progression of PCa and its outcome for the patient. The role of abundant PPAT on other prostate-related disorders has not yet been investigated. The biological mechanisms that result in the expansion of this AT in patients with abundant PPAT are still unknown, limiting our ability to formulate hypotheses regarding its role in PCa progression.

In this study, we first developed a more refined definition of abundant PPAT that takes into account the correlation between PPAT and prostate volume demonstrated in previous studies [17,18]. Using this definition, we validated the notion that PPAT abundance correlated with PCa aggressiveness, as described in previous studies [6,10–16], and used these validated samples to characterize their biological characteristics. We showed that abundant PPAT exhibited extensive ECM remodeling, notably of the collagen network, decreasing the mechanical constraints in hypertrophic adipocytes, leading to an inflammation-free expansion. Degradation of the most abundant collagen in AT, collagen VI (COL6), was associated with increased production of endotrophin (ETP), a signaling peptide derived from AT [19]. We further confirmed that ETP was elevated in the urine of patients with abundant PPAT, showing that ECM remodeling exists at the clinical level. This first functional and structural biological characterization of PPAT points to an unusual mechanism of AT expansion based on the reshaping of the ECM and opens new avenues to explain its role in prostate disorders.

Materials and methods

Study approval

The study was conducted in accordance with the guidelines and with the full approval of the National Ethics Committee (AC-2020-4031). Participants provided written informed consent before being included in the study, which was conducted in accordance with the Declaration of Helsinki principles as revised in 2000.

Patients, prostate, and fat measurements

Between September 2016 and July 2021, patients with localized PCa diagnosed by prostate biopsies undergoing radical prostatectomy (RP) were recruited. Patients with metastatic PCa (as assessed by computerized tomography and/or bone scan) or prior treatment (radiotherapy, hormonal, or high-intensity ultrasound treatment) were excluded. All patients underwent preoperative 1.5T multiparametric magnetic resonance imaging (mpMRI), including anatomic three-dimensional (3D) fast spin echo T2-weighted MRI, functional diffusion-weighted MRI, and dynamic contrast-enhanced MRI, after injection with 20 mg butyl scopolamine (Buscopan; Boehringer-Ingelheim, Paris, France). mpMRI data were anonymized, then the PPAT and prostate volume and the subcutaneous and perirectal AT areas were measured using a semiautomated segmentation technique on contiguous 3-mm T2-weighted axial slices and Olea Sphere software (Olea medical, La Ciotat, France). The subcutaneous AT area was determined by measuring the perpendicular distance between the skin and the anterior upper border of the symphysis pubis on a selected T2-weighted axial slice where it was maximum. The perirectal AT area was determined by segmenting the fat around the rectum at the level of the apex of the prostate (supplementary material, Table S1). Twenty patients with negative mpMRI results (named 'no cancer') were included for comparison of PPAT and prostate volume. All segmentations and measurements were performed by three trained observers blinded to the clinical and pathological data. The PPAT was segmented from the level of the prostate base to the apex (Figure 1A) (mean 14 slices per patient) as previously described [8]. Clinical data, including age, BMI, serum prostate-specific antigen (PSA) concentration, and pathological parameters of the tumor on RP pieces: tumor volume, Gleason score, International Society of Urological Pathology (ISUP) group (histological score reflecting the differentiation of PCa determined by a trained pathologist according to the 2016 World Health Organization classification and ISUP recommendations), percentage of high-grade lesions (defined as the percentage of a tumor with a Gleason score > 4), pathological T (pT) stage, and extraprostatic extension, were acquired from medical records. Preoperative biopsy Gleason and ISUP scores were also recorded. Full clinical characteristics of the cohort are provided in supplementary material, Table S2.

PPAT collection and tissue processing

PPATs were removed from patients undergoing RP, and the samples were anonymized. Charred samples were excluded from the study. Samples were transported in DMEM (Thermo Fisher Scientific, Courtaboeuf, France) to the research lab within 1 h, weighed, and processed

© 2026 The Pathological Society of Great Britain and Ireland. www.pathsoc.org

10969896, 0, Downloaded from https://pathsocjournals.onlinelibrary.wiley.com/doi/10.1002/path.70033 by Ut Southwestern Medical Center, Wiley Online Library on [20/02/2026]. See the Terms and Conditions (https://onlinelibrary.wiley.com/terms-and-conditions) on Wiley Online Library for rules of use; OA articles are governed by the applicable Creative Commons License

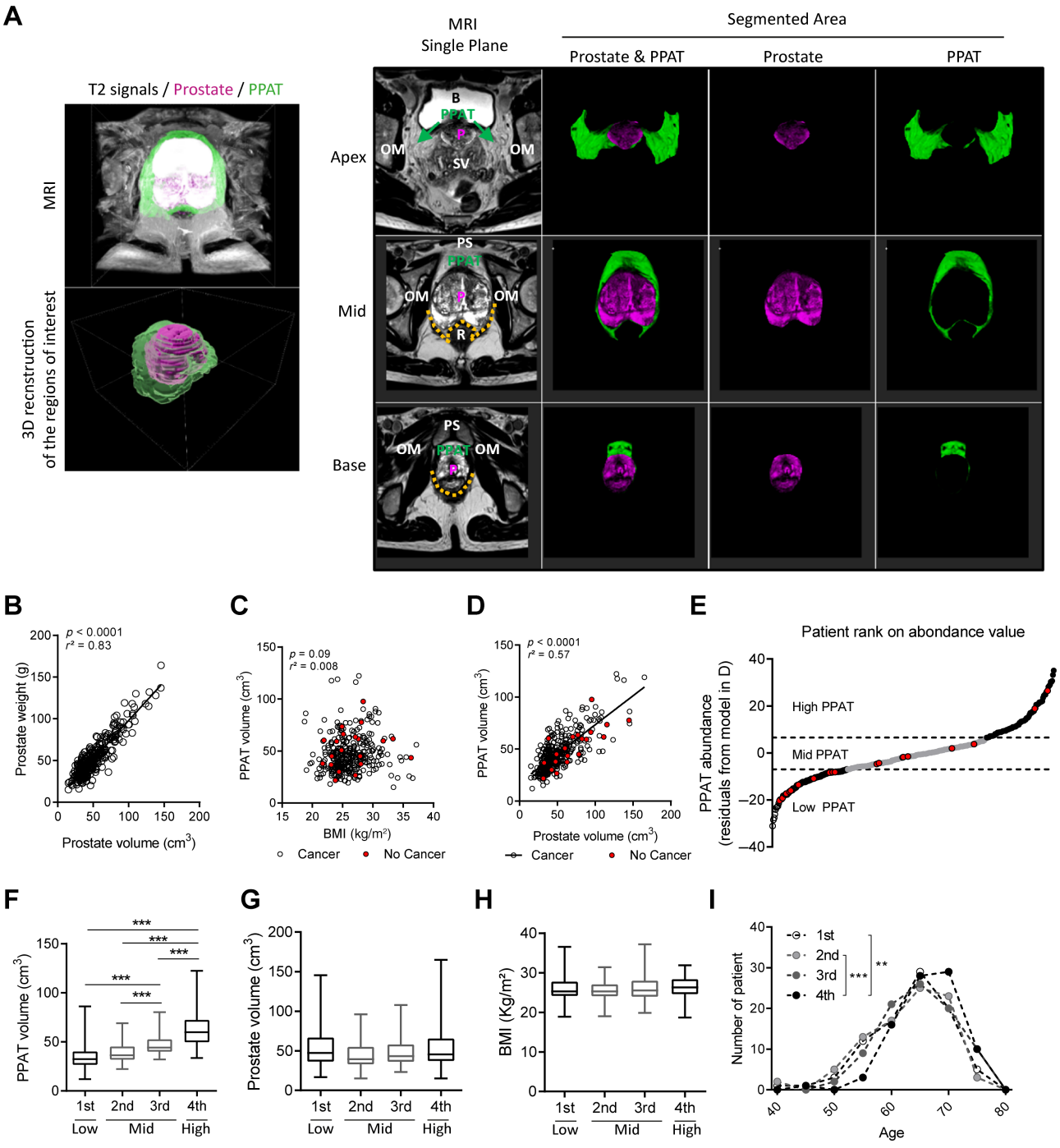

Figure 1. A new statistical approach to defining abundant PPAT relative to prostate volume. (A) Left panel: representative 3D projection and reconstruction of axial sections from T2-weighted mpMRI signals and regions of interest delineating prostate (pink) and PPAT (green); right panel: single axial MRI sections from base, middle, and apex of the prostate. The localization of PPAT, prostate (P), and the anatomical limits of PPAT are shown on single axial MRI section (B, bladder; OM, obturator muscle; P, prostate; PPAT, Periprostatic Adipose Tissue; PS, pubic symphysis; R, rectum; SV, seminal vesicle; orange dotted lines indicate Denonvillier's fascia). Segmented area represents the region of interest delineating the prostate (pink) and the PPAT (green) for each single MRI section presented. (B) Correlation between prostate weight recorded after prostatectomy and prostate volume measured on mpMRI ($n = 351$). Linear regression was used to draw the slope of best fit, and linear correlation coefficient (r^2) and p value are indicated (p). (C) Lack of correlation between prostate volume and BMI of patient ($n = 371$); patients without PCa are indicated in red. (D) Correlation between PPAT and prostate volume ($n = 371$); patients without PCa are indicated in red. Linear regression was used to draw the slope of best fit, and linear correlation coefficient (r^2) and p value are indicated (p). (E) Scatter plot of patients ranked according to PPAT abundance showing patients with low, mid, and high PPAT abundance. PPAT abundance was calculated from residual value for each patient with respect to linear regression model in panel D ($n = 371$); patients without PCa are indicated in red. (F) PPAT volume measured on MRI according to abundance quartile ($n = 86–87$ per quartile). (G) Prostate volume of patients in each abundance quartile ($n = 86–87$ per quartile). (H) BMI of patients in each abundance quartile ($n = 86–87$ per quartile). (I) Distribution of patients' age in each abundance quartile ($n = 86–87$ per quartile). Individual patient's data are indicated by dots, bars indicate means ± SEM. Statistical differences between groups were evaluated by ANOVA followed by a post-test for linear trend and for nonnormally distributed data, the Kruskal–Wallis test with Dunn's multiple comparisons *post hoc* test was applied (**$p < 0.01$; ***$p < 0.001$).

© 2026 The Pathological Society of Great Britain and Ireland. www.pathsoc.org

10969896, 0, Downloaded from https://pathsocjournals.onlinelibrary.wiley.com/doi/10.1002/path.70033 by Ut Southwestern Medical Center, Wiley Online Library on [20/02/2026]. See the Terms and Conditions (https://onlinelibrary.wiley.com/terms-and-conditions) on Wiley Online Library for rules of use; OA articles are governed by the applicable Creative Commons License

for downstream applications. For RT-qPCR analysis and measurement of MMP9 activity and of hydroxyproline content, PPATs were snap-frozen in liquid nitrogen and stored at −80 °C. For 3D microscopy, samples were fixed with 4% paraformaldehyde at room temperature (RT) for 24 h. Some of the samples were also used to isolate adipocytes and the SVF after collagenase digestion or to prepare PPAT-conditioned medium as previously described [8].

Flow cytometry analysis

Isolation of SVF and flow cytometry were performed as described previously [20]. The antibodies used are listed in supplementary material, Table S3.

ELISA assays

A panel of secreted adipokines was assessed in PPAT-conditioned medium using an ELISA kit as described previously [8]. ETP was quantified in plasma collected before prostate massage and urine collected after prostate massage using a homemade ELISA as described previously [21].

RNA extraction and RT-qPCR

RNA extraction and RT-qPCR were performed as described previously [8]. The primers used are listed in supplementary material, Table S4.

Sample preparation for proteomic analysis

Proteins were extracted from 500 µl of adipocytes washed in PBS with 500 µl 1× RIPA buffer (Sigma-Aldrich, Saint Quentin Fallavier, France) supplemented with complete antiprotease tablet (Sigma-Aldrich) with a Precellys tissue homogenizer and ceramic beads (CK14) (Bertin Technologies, Montigny-le-Bretonneux, France). After centrifugation, the extract was recovered, with the top layer not containing the lipids, and centrifuged again. Protein concentration was determined using DC protein assay kit (Biorad, Marnes-la-Coquette, France) following the manufacturer's instructions. Then 40 µg proteins were digested for characterization by mass spectrometry using an S-Trap micro-spin column (ProtiFi, NY, USA).

LC–MS/MS analysis

Peptides were analyzed by liquid chromatography–tandem mass spectrometry (LC–MS/MS) using an Orbitrap Q Exactive HF-X mass spectrometer (Thermo Fisher Scientific, Illkirch-Graffenstaden, France). The mass spectrometer was operated in data-dependent acquisition mode with Xcalibur software. Full technical details are provided in Supplementary materials and methods.

Bioinformatic MS data analysis

Raw MS and MS/MS data were analyzed using Mascot (version 2.6.1, http://matrixscience.com) against the Human UniProtKB database (Swiss-Prot/TrEmbl, 556,568 entries). Proline software (version 1.6, http://proline.profiproteomics.fr/) was used for the validation of identifications and the label-free quantification of identified proteins [22] (detailed in Supplementary materials and methods). Differential analysis was performed with limma (version 3.40.6) from Bioconductor and FactoMineR (version 2.4) package in R (version 3.6). Gene Ontology (GO) term enrichment analysis was performed with the Molecular Signature Database on differentially represented proteins (version 7.4 MSigDB). The MS proteomics data were deposited at the ProteomeXchange Consortium via the PRIDE partner repository with the dataset identifier PXD038514. Protein abundances from proteomic data are available in supplementary material, Table S9, and a list of the Top 10 under- and over-represented proteins identified by spectrometry-based proteomics in high PPAT relative to low PPAT is presented in supplementary material, Table S10.

3D confocal microscopy and quantification

For immunofluorescence staining, PPATs (250 mg) were fixed and stained as described previously [8]. For Fluorescent Collagen Hydridizing Peptides (F-CHPs), fixed ATs were incubated with 20 µm F-CHPs overnight at 4 °C and washed with PBS. Z-stack images were acquired using an LSM710 confocal microscope with 40× objective. Staining was quantified using Imaris software (version 9.2). Picrosirius Red staining was performed as described previously [8]. The antibodies used are listed in supplementary material, Table S5.

Hydroxyproline quantification

Hydroxyproline quantification was performed as described previously [8].

MMP9 activity

Active MMP9 levels were quantified in 200 µg total protein using the Human Active MMP-9 Fluorokine E assay kit (F9M00; R&D Systems, Noyal Châtillon sur Seiche, France) following the manufacturer's instructions. Fluorescence was quantified using the FLX800 fluorimeter with excitation at 340 nm and emission measured at 405 nm.

Statistics

Univariate statistical analysis of clinical data was performed using ANOVA for continuous variables or using the chi-squared test for qualitative variables within Prism (version 5.04). Linear regression was computed with Prism version 5.04, and residuals were calculated according to the fitted linear model. Multivariate analysis was performed by multiple logistic regression using the glm function in R (version 3.6) to predict patients having an ISUP score above or equal to 3. For experimental data, statistical analysis was performed using Student's *t*-test after testing for normality using a Kolgomorov–Smirnov test for comparison between two groups. For comparisons among three or more groups, ANOVA followed by a test

© 2026 The Pathological Society of Great Britain and Ireland. www.pathsoc.org

10969896, 0, Downloaded from https://pathsocjournals.onlinelibrary.wiley.com/doi/10.1002/path.70033 by Ut Southwestern Medical Center, Wiley Online Library on [20/02/2026]. See the Terms and Conditions (https://onlinelibrary.wiley.com/terms-and-conditions) on Wiley Online Library for rules of use; OA articles are governed by the applicable Creative Commons License

for linear trends was used when normality was assumed, whereas the Kruskal–Wallis test with Dunn's *post hoc* test was applied for nonparametric data. Statistical differences were considered significant if the p value < 0.05.

Results

A new statistical approach to defining abundant PPAT

As PPAT volume has been reported to correlate with prostate volume, recent studies have used the ratio of PPAT volume to prostate volume in an individual – the normalized periprostatic fat volume (NPFV) – to compare PPAT abundance between individuals in order to better define the relative fat volume in the periprostatic area [17,18]. To improve this definition, we developed a measure that expresses the volume of PPAT with respect to the volume of the prostate normalized to a population rather than to an individual. We first used a cohort of 351 patients awaiting prostatectomy for PCa using preoperative mpMRI, from which we measured prostate and PPAT volume within well-defined anatomical limits (supplementary material, Table S1 and Figure 1A). We found a strong correlation between the volume of the prostate determined by mpMRI before prostatectomy and its weight after prostatectomy (Figure 1B), validating the accuracy of the measurement method. A group of 20 patients that underwent mpMRI for nononcological pathologies were also included in the study. In all patients (with or without cancer), PPAT volume was independent of BMI (Figure 1C) and correlated with prostate volume (Figure 1D).

As expected, both subcutaneous AT area (supplementary material, Figure S1A) and perirectal AT area (supplementary material, Figure S1B) correlated with BMI in the cohort. Of note, the correlation between BMI and subcutaneous AT area was stronger than with perirectal AT area, as already described for visceral AT [23]. Based on this strong correlation between PPAT volume and prostate volume, we modeled the expected PPAT volume according to the prostate volume using a linear regression model and calculated PPAT abundance with the residual values from this model. The residual values represent the difference between the volume of PPAT quantified by mpMRI and the amount of PPAT predicted by the model (Figure 1E). The cohort was divided into quartiles according to residual values, allowing the identification of patients with the least PPAT in the first quartile (low PPAT) and patients with the most PPAT in the fourth quartile (high PPAT) (Figure 1E,F). Patients in the second and third quartiles were classified as having a mid PPAT abundance (Figure 1E,F). No differences were observed between patients in the four quartiles when we analyzed prostate volume (Figure 1G) and BMI (Figure 1H), but there was a significant trend toward older age in the fourth quartile compared to the first and second (Figure 1I).

In our PCa cohort, NPFV only partially reflected PPAT abundance as estimated by our regression model (supplementary material, Figure S2A). Patient ranking by NPFV frequently diverged from PPAT grouping, with ∼30% of patients classified differently by the two methods (supplementary material, Figure S2A). To examine this further, patients were divided into NPFV quartiles (first = low, second and third = mid, fourth = high). PPAT volumes did not differ across quartiles (supplementary material, Figure S2B), whereas prostate volume decreased with increasing NPFV (supplementary material, Figure S2C). Thus, large NPFVs are due primarily to small prostate volumes rather than large PPAT volumes, unlike our model.

We then validated in our cohort (whose clinical and biological parameters are presented in supplementary material, Table S2) the relationship between PPAT abundance, as defined earlier, and PCa aggressiveness. Of note, this cohort included only patients who had undergone prostatectomy, since the structural and functional characterization of abundant compared to low PPAT was the goal of our study. Therefore, the cohort was rather homogeneous in the aggressiveness of cancers, according to prostatectomy indications [24]. Most patients in our PCa cohort were graded 2 or 3 on the ISUP scale (supplementary material, Table S2). Nevertheless, the proportion of patients with an ISUP grade ≥3 increased with PPAT abundance and was significantly different between the low- and high-PPAT groups (supplementary material, Figure S3A and Table S6). In addition to the ISUP score, the percentage of high-grade lesions in the tumors of patients in the high-PPAT group was significantly greater than in patients in the low-PPAT group (supplementary material, Figure S3B and Table S6). Moreover, there was a significant association between the abundance of PPAT and the concentration of prostate-specific antigen in the blood of patients with PCa prior to surgery (supplementary material, Table S6). Multivariate analysis using a logistic regression model found that PPAT abundance was an independent risk factor for PCa with an ISUP score ≥3 (supplementary material, Figure S3C), whereas NPFV was not (supplementary material, Figure S2D). Therefore, these results, in accordance with the literature [6,10–16], validated our ranking of PPAT abundance. We then characterized its biological characteristics.

PPAT expands by adipocyte hypertrophy with no associated inflammation

AT expands in response to surplus energy by two main mechanisms: adipocyte enlargement, or hypertrophy, and adipocyte hyperplasia, in which new adipocytes are recruited by adipogenesis from progenitors [25]. The balance between hypertrophy and hyperplasia depends on the adipose depot concerned [25]. Paraffin-embedded PPAT sections stained with H&E were used to assess the diameter of adipocytes using a semiautomated method, Adiposoft (https://imagej.net/plugins/adiposoft) (Figure 2A). The adipocyte size distribution curve was shifted toward larger cells in PPAT from patients in the high-PPAT group compared with those in the low-PPAT group, and the mean adipocyte

© 2026 The Pathological Society of Great Britain and Ireland. www.pathsoc.org

10969896, 0, Downloaded from https://pathsocjournals.onlinelibrary.wiley.com/doi/10.1002/path.70033 by Ut Southwestern Medical Center, Wiley Online Library on [20/02/2026]. See the Terms and Conditions (https://onlinelibrary.wiley.com/terms-and-conditions) on Wiley Online Library for rules of use; OA articles are governed by the applicable Creative Commons License

diameter was larger (Figure 2B), indicating adipocyte hypertrophy. To quantify adipose progenitors in the SVF, cells were immunostained with antibodies against the markers CD45, CD34, and CD31 and analyzed by flow cytometry. The percentage of cells in this fraction that were progenitor cells (defined as CD45−/CD34+/CD31− cells) was similar in PPAT from patients in the various groups (Figure 2C). Furthermore, when additional markers (MSCA1 and CD271) were used to characterize the subpopulations of adipose progenitors [20], the proportions of the various progenitor subsets (the adipogenic MSCA1+, myofibrogenic MSCA1−/CD271+, and immature MSCA1/CD271− subsets) were similar in all groups (supplementary material, Figure S4A),

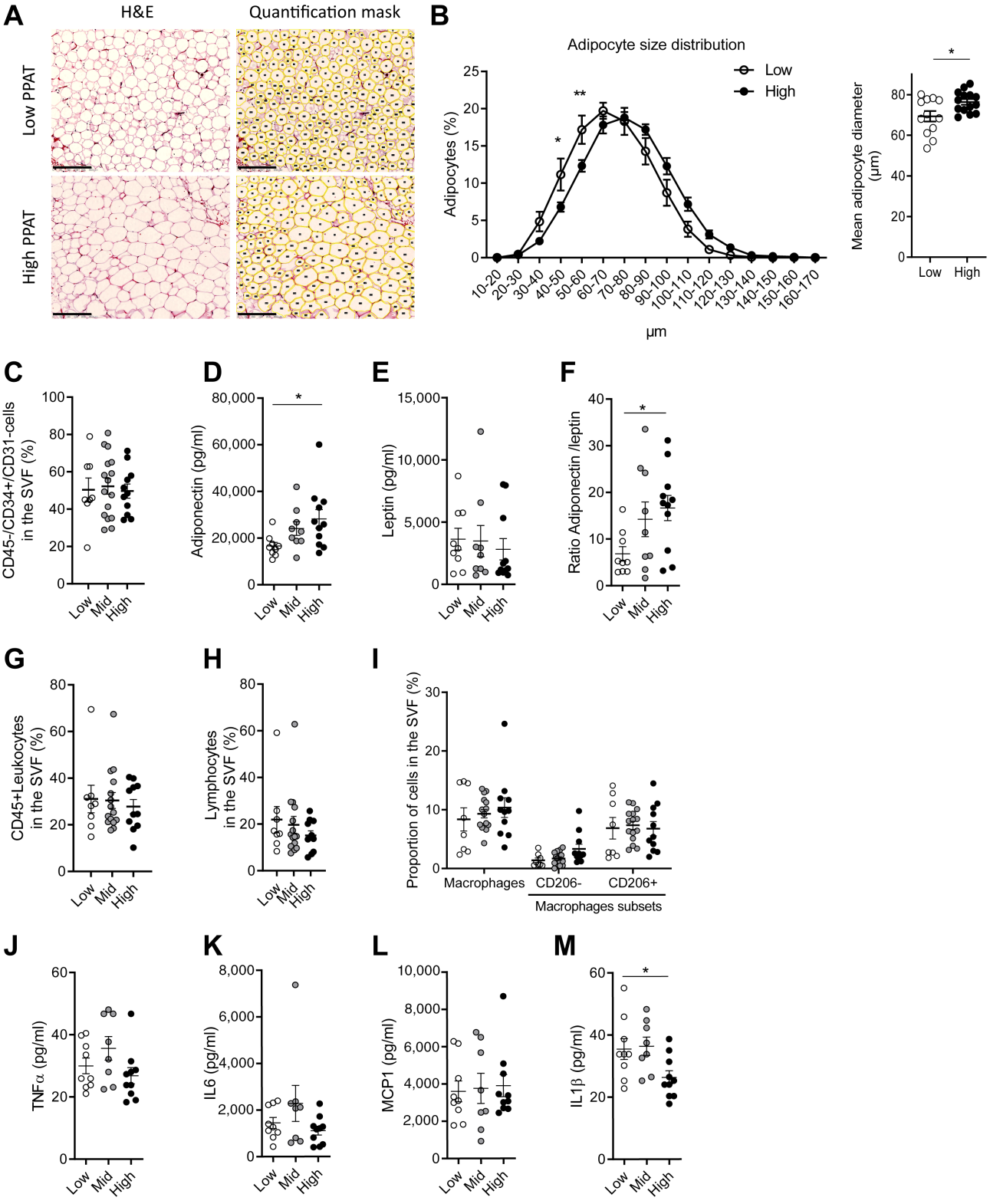

Figure 2 Legend on next page.

© 2026 The Pathological Society of Great Britain and Ireland. www.pathsoc.org

10969896, 0, Downloaded from https://pathsocjournals.onlinelibrary.wiley.com/doi/10.1002/path.70033 by Ut Southwestern Medical Center, Wiley Online Library on [20/02/2026]. See the Terms and Conditions (https://onlinelibrary.wiley.com/terms-and-conditions) on Wiley Online Library for rules of use; OA articles are governed by the applicable Creative Commons License

indicating no increase in progenitors in abundant PPAT. We conclude that adipocyte hypertrophy rather than hyperplasia was the mechanism of PPAT expansion in patients with abundant PPAT.

Adipocyte hypertrophy during AT expansion is usually associated with changes in secretion related to AT dysfunction [2,3]. Key among these changes is increased secretion of leptin and, in parallel, decreased secretion of adiponectin [2,3]. The decrease in the ratio of adiponectin/leptin secretion has been proposed as a marker of dysfunctional AT in metabolic disorders and inflammation [2,3]. Despite the adipocyte hypertrophy we saw in PPAT from patients in the high-PPAT group, more adiponectin was secreted by this PPAT than by PPAT from patients in the low-PPAT group (Figure 2D), whereas leptin secretion by both tissues was similar (Figure 2E). Accordingly, the adiponectin/leptin secretion ratio was greater in high than in low PPAT (Figure 2F). Thus, the adipocyte hypertrophy observed in high PPAT is not associated with the changes in secretion that are usually observed in dysfunctional AT.

The proportion of immune system cells in AT generally increases as the tissue expands, and this is associated with the onset of chronic low-grade inflammation [26]. We measured the proportion of immune cells in PPAT from patients in the three groups by immunostaining the cells in the SVF with antibodies against CD45 and other specific markers of immune population subsets and analyzed them by flow cytometry. The proportion of CD45+ leukocytes in this fraction was similar in the various groups of patients (Figure 2G), as was the proportion of total lymphocytes (defined as CD45+/low side scatter) (Figure 2H) and of various lymphocyte subsets (supplementary material, Figure S4B). The proportion of macrophages (defined as CD45+/CD14+ cells), including the subpopulations that express or do not express CD206, were also similar in the various groups (Figure 2I). These data indicate that PPAT expansion is not associated with increased immune cell infiltration.

To further characterize the inflammatory state of abundant PPAT, we quantified secretion of several proinflammatory cytokines by PPAT from patients in the various groups. No significant differences were seen between the amounts of TNFα, IL6, or MCP-1 secreted (Figure 2J–L), and the tissue from patients in the high PPAT group secreted slightly less IL1β than the others (Figure 2M). Thus, the PPAT from patients in the high-PPAT group does not secrete more proinflammatory cytokines than the PPAT from the patients in the mid- and low-PPAT groups. Together, these data indicate that, although PPAT expands by adipocyte hypertrophy, this expansion does not cause the inflammation observed in other ATs that expand by this mechanism.

Under-representation of mechano-sensing proteins in adipocytes from abundant PPAT

According to our findings described earlier, adipocytes are the main cell type that changes in the PPAT from patients in the high-PPAT group. Adipocytes from high- and low-PPAT groups were isolated and analyzed by proteomic approaches. Principal component analysis of the proteomic dataset separated patients according to the abundance of their PPAT (Figure 3A). Component 1, which separated the patients according to their PPAT groups, explained 52% of the variance in the proteomic dataset (Figure 3A). Whereas the low-PPAT patients grouped closely on the scatter plot, those with high PPAT spread widely (Figure 3A). Of the 4,033 proteins identified by proteomic analysis, statistical analysis found 352 whose abundance differed in PPAT from patients in the high- and low-PPAT groups: 157 were over-represented and 195 were under-represented in the samples from the high-PPAT group compared to those from the low-PPAT group (Figure 3B). Hierarchical clustering using Ward's method on differentially represented proteins grouped the samples according to their abundance status (Figure 3C).

To further characterize the differences between adipocytes in the PPAT of patients in the high- and low-PPAT groups, we used GO enrichment analysis of the proteomic dataset to identify cellular components and molecular functions. We found large differences in the abundance of proteins involved in cytoskeletal organization, cell–ECM interactions, and, to a lesser extent, lipid metabolism (Figure 3D). From this analysis, the main characteristics of adipocytes from abundant PPAT can be described as having, above all, an under-representation of proteins involved in mechano-transduction and sensing stiffness (ontology terms in

Figure 2. PPAT expands by adipocyte hypertrophy with no associated inflammation. (A) Representative images of PPAT sections stained with H&E and used to quantify adipocyte diameter in PPAT from patients in low and high groups. The corresponding quantification mask is shown. Scale bars, 250 μm. (B) Size distribution (left panel) and mean diameters (right panel) of adipocytes in PPAT from patients in low ($n = 12$) and high ($n = 14$) groups. (C) Percentage of progenitor cells (CD45−/CD34+/CD31−) in SVF of PPAT from patients in low ($n = 8$), mid ($n = 16$), and high ($n = 11$) groups, as quantified by flow cytometry. (D–F) Quantification of concentration of adiponectin (D) and leptin (E) in conditioned medium of PPAT from patients in low ($n = 9$), mid ($n = 9$), and high ($n = 11$) groups, and adiponectin-to-leptin ratio (F). (G) Percentage of cells in SVF of PPAT from patients in low ($n = 8$), mid ($n = 15$), and high ($n = 11$) groups that are CD45+ leukocytes. (H) Percentage of cells as in (G) that are low FSC/low SSC/CD45+/CD3+ T cells in low ($n = 8$), mid ($n = 15$), and high ($n = 11$) groups. (I) Percentage of cells as in (G) that are CD45+/CD14+ macrophages (all macrophages), CD45+/CD14+/CD206− recruited macrophages (CD206−), or CD45+/CD14+/CD206+ resident macrophages (CD206+) in low ($n = 8$), mid ($n = 15$), and high ($n = 11$) groups. All percentages in (G)–(I) were quantified by flow cytometry. (J–M) Quantification of concentrations of TNFα (J), IL6 (K), MCP1 (L), and IL1β (M) in conditioned medium of PPAT from patients in low, mid, and high groups ($n = 8$–10). Bars indicate means ± SEM. Two-way ANOVA followed by Bonferroni post-test was used to analyze adipocyte diameter. Other statistical differences were evaluated by ANOVA with post-test for linear trend (*$p < 0.05$; **$p < 0.01$).

© 2026 The Pathological Society of Great Britain and Ireland. www.pathsoc.org

10969896, 0, Downloaded from https://pathsocjournals.onlinelibrary.wiley.com/doi/10.1002/path.70033 by Ut Southwestern Medical Center, Wiley Online Library on [20/02/2026]. See the Terms and Conditions (https://onlinelibrary.wiley.com/terms-and-conditions) on Wiley Online Library for rules of use; OA articles are governed by the applicable Creative Commons License

bold in Figure 3D). Among them, yes-associated protein 1 (YAP1) is the most under-represented protein in the PPAT of patients in the high-PPAT group (log2 fold-change = −5.8) compared with the low-PPAT group (Figure 3E). YAP1 is a key mechano-transducer that senses mechanical stimuli and relays them to regulate transcription and, thus, many aspects of cell behavior [27]. ZYXIN [28] and PACSIN2 [29], proteins that participate in the nuclear translocation and activation of YAP1 upon mechanical stress, were also significantly under-represented in the most abundant PPAT, as was ROCK2, a target of the YAP/TEAD transcriptional complex [27] (Figure 3E). We confirmed by immunofluorescence microscopy that PPAT from patients in the high-PPAT group contained much less YAP1 than that from patients in the low-PPAT group (Figure 3F).

The second important characteristic of adipocytes from abundant PPAT identified by pathway enrichment analysis was under-representation of several tubulin isoforms (Figure 3G), which was accompanied by altered microtubule organization seen by immunofluorescence microscopy (Figure 3H). Proteins involved in cytoskeletal organization, such as cortactin (CTTN), an actin nucleation factor that influences the stability of actin filaments, and members of the vinexin family (SORBS-1 and SORBS-3), which are involved in contractile force generation in response to mechanical stress [30], were also under-represented (Figure 3I).

A third notable characteristic of adipocytes from the high-PPAT group was the abundance of proteins involved in lipid metabolism (Figure 3D), which may explain, at least in part, the observed adipocyte hypertrophy. Several key proteins involved in lipolysis were under-represented in PPAT from patients in the high-PPAT group, including adipocyte triglyceride lipase (encoded by *PNPLA2*), hormone-sensitive lipase (encoded by *LIPE*), perilipin1 (encoded by *PLIN1*), and abhydrolase domain-containing protein 5 (encoded by *ABHD5*) (supplementary material, Figure S5A). For *PNPLA2* and *LIPE*, a downward trend regulation at mRNA levels according to abundance status was confirmed by RT-qPCR, whereas the level of *MGLL* (encoding monoacylglycerol lipase) was unchanged (supplementary material, Figure S5B). By contrast, adiponectin (encoded by *ADIPOQ*) and several lipid transporters that take up fatty acids like CD36 or FABP4 (fatty acid binding protein 4) were over-represented (supplementary material, Figure S5A). Regulation of their mRNA levels according to abundance status was confirmed by RT-qPCR, and similar differences were also observed for the long-chain fatty acid transport protein 4 (encoded by *SLC27A4*) (supplementary material, Figure S5C).

The collagen network in abundant PPAT is relatively loose

The under-representation of proteins involved in mechano-sensing and cytoskeletal contractile force generation in abundant PPAT suggest that these PPATs might be subject to fewer mechanical constraints by ECM than less abundant PPAT, which may account for its expansion without inflammation. To investigate this hypothesis, we stained the collagen fibers using Picrosirius Red, imaged the staining by 3D confocal microscopy, and reconstructed images of the fiber network in 3D. In the reconstructions, the signal from collagen fibers was weaker in PPAT from patients in the high-PPAT group than it was in the patients in the low-PPAT group (as shown by the maximum intensity projection), and the collagen network was substantially less dense and had thinner fibers (Figure 4A). These observations were verified using Imaris software to quantify the volume and length of the collagen fibers as well as the total number of branches seen in the 3D reconstructions (Figure 4B–D). To further confirm our findings, we used a different approach based on quantification of hydroxyproline, a component of collagen that comprises around 13.5% of its amino acid composition. Consistent with the imaging analysis of the collagen fiber network, we found significantly less hydroxyproline in PPAT from patients in the high-PPAT group than in patients in the low-PPAT group (Figure 4E). Taken together, these analyses indicate that abundant PPAT has a looser collagen network than less abundant PPAT, supporting the hypothesis that mature adipocytes in abundant PPAT are subject to fewer mechanical constraints than those in less abundant PPAT.

Abundant PPAT exhibits increased collagen degradation likely by MMP9

Our findings indicate that abundant PPAT contains less collagen, organized in a looser network, than in less abundant PPAT. To determine whether this reflects less collagen synthesis or more degradation of the proteins, we used RT-qPCR to compare the expression of the genes encoding the major fibrillar collagens (*COL1A1* and *COL3A1*) as well as the three different alpha chains of the most abundant nonfibrillar collagen, collagen VI [31] (*COL6A1*, *COL6A2*, and *COL6A3*) in PPAT from patients in the high- and low-PPAT groups. We saw no differences between them (Figure 5A), suggesting that the smaller amount of collagen and looser network in abundant PPAT is not due to less synthesis but may be due to increased degradation. To investigate this hypothesis, we stained PPAT samples with a fluorescent peptide (F-CHP) that binds specifically to denatured collagen strands [32] and imaged the staining by 3D confocal microscopy. The images showed a punctate staining located alongside fibrillar structures in PPAT from patients in the high-PPAT group, whereas very weak signals were seen in PPAT from patients in the low-PPAT group (Figure 5B, left panel). Quantification of the signals from F-CHP after 3D reconstruction confirmed the substantial increase in collagen degradation in PPAT from the high-PPAT group compared with the low-PPAT group (Figure 5B, right panel).

© 2026 The Pathological Society of Great Britain and Ireland. www.pathsoc.org

10969896, 0, Downloaded from https://pathsocjournals.onlinelibrary.wiley.com/doi/10.1002/path.70033 by Ut Southwestern Medical Center, Wiley Online Library on [20/02/2026]. See the Terms and Conditions (https://onlinelibrary.wiley.com/terms-and-conditions) on Wiley Online Library for rules of use; OA articles are governed by the applicable Creative Commons License

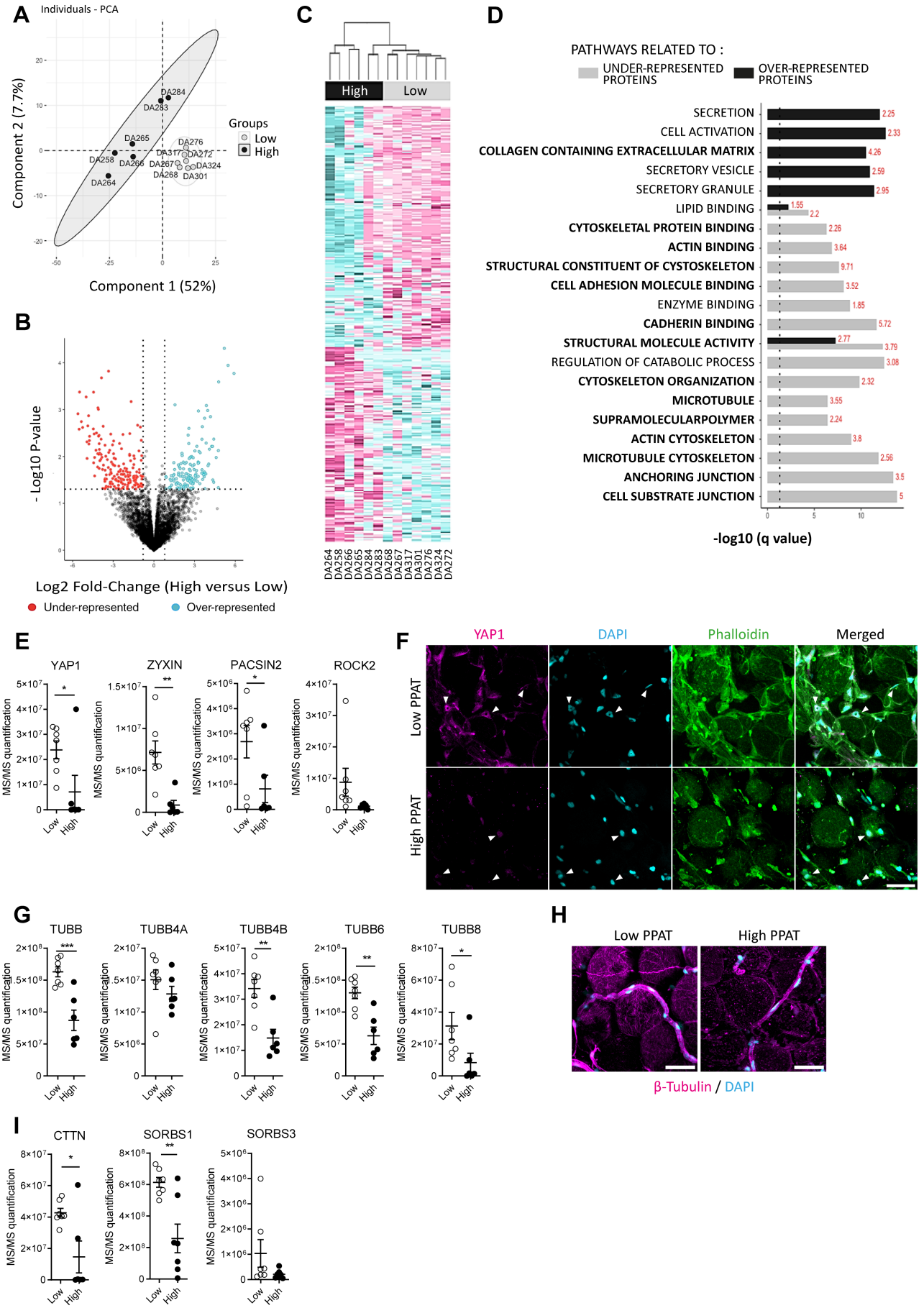

Figure 3 Legend on next page.

© 2026 The Pathological Society of Great Britain and Ireland. www.pathsoc.org

10969896, 0, Downloaded from https://pathsocjournals.onlinelibrary.wiley.com/doi/10.1002/path.70033 by Ut Southwestern Medical Center, Wiley Online Library on [20/02/2026]. See the Terms and Conditions (https://onlinelibrary.wiley.com/terms-and-conditions) on Wiley Online Library for rules of use; OA articles are governed by the applicable Creative Commons License

Matrix metalloproteinases (MMP) are the main enzymes involved in collagen degradation. To investigate the potential involvement of various MMP in the degradation of collagen in high PPAT, we quantified the expression of the main metalloproteinase genes expressed in AT (*MMP2*, *MMP9*, *MMP11*, *MMP14*, and *BMP1*) by RT-qPCR. Significantly more *MMP9* mRNA was found in PPAT from patients in the high-PPAT group than in PPAT from patients in the low-PPAT group (Figure 5C). This was confirmed by analysis of the proteomics data from isolated adipocytes (Figure 5D), and it was reflected in elevated MMP9 activity (Figure 5E). However, MMP9 activity and mRNA expression in abundant PPAT seem bimodal, suggesting that in some patients, ECM remodeling could be independent of MMP9. MMP activity is tightly regulated by the balance between the expression of the genes encoding MMPs and their endogenous inhibitors, the tissue inhibitors of metalloproteinases (TIMPs). Therefore, we analyzed the expression of the genes encoding various TIMP isoforms as well as those encoding the lysyl oxidases LOX and LOXL1, which cross-link ECM proteins. All of these genes were expressed at similar levels in the high- and low-PPAT groups (supplementary material, Figure S6). We conclude that the smaller amount of collagen in abundant PPAT than in less abundant PPAT and its disorganization is due to enhanced degradation that likely involves MMP9.

COLVI remodeling is associated with high ETP production in abundant PPAT

Collagen VI is a highly enriched ECM component of AT [31]. We investigated whether COLVI was also subjected to degradation in abundant PPATs by immunofluorescence staining and 3D confocal microscopy. As seen in Figure 6A, the COLVI staining was weaker in the high-PPAT group than in the low-PPAT group, it was punctiform, and the COLVI microfibrils were clearly disorganized, confirming that COLVI is degraded in abundant PPAT. The proteolytic cleavage of the C-terminal part of COL6A3 generates a bioactive fragment called ETP that promotes a wide range of cellular and tissular responses leading to abnormal tissue remodeling, fibrosis, and inflammation or tumor progression [19]. We then investigated whether ETP generation was increased in abundant PPAT. Tissues were stained with an antibody specific for ETP [21,33] and imaged by immunofluorescence microscopy (Figure 6B). Expression of ETP was increased in the high- compared to the low-PPAT group (Figure 6B). To investigate the clinical relevance of our findings, we quantified ETP in biological fluids from patients that had undergone mpMRI for PCa diagnosis (see supplementary material, Tables S7,S8 for descriptions of the new cohort). The patients were classified into the low-, mid-, and high-PPAT groups defined previously. ETP plasma levels were similar in all patients regardless of their PPAT abundance status (Figure 6C). By contrast, the ETP concentration in urine collected after prostate massage, which promotes the exfoliation of epithelial and stromal cells, as well as the release of prostate-derived proteins and other biomolecules into urine [34], was greater in patients in the high-PPAT group than it was in patients in the low-PPAT group (Figure 6D). These results confirm the clinical relevance of our findings on ECM remodeling in PPAT from prostatectomy specimens.

Discussion

In this work, we first developed a new approach to define PPAT abundance using mpMRI, the gold standard for imaging prostate and surrounding tissues, to measure both prostate and PPAT volume rather than fat thickness or the area of the tissue at a single point. Slice-by-slice segmentation was applied as in our previous work [8]. Consistent with earlier studies [17,18], PPAT volume correlated with prostate size. As prostate size is highly variable between individuals and often increases with age [35], it is important to take this parameter into account to accurately define the relative fat volume in the periprostatic area. Previous studies used NPFV, but this can bias results toward smaller prostates [17], as we also observed in our study. To overcome this, we applied a linear regression model that normalizes PPAT

Figure 3. Under-representation of mechano-sensing proteins in adipocytes from abundant PPAT. (A) Principal component analysis of proteomics datasets from adipocytes isolated from PPAT of individual patients (each indicated by a dot and a label) in low and high groups ($n = 6$ or 7 per group). Ellipses indicate grouping according to PPAT abundance. (B) Volcano plot representing log2 fold-change of relative protein representation in proteomics dataset and $-$log10 of p value calculated using limma differential expression analysis ($n = 6$–7 per group), showing under-represented (pink) and over-represented (green) proteins. (C) Hierarchical clustering of differentially under-represented (pink) and over-represented (green) proteins in PPAT of patients in low (gray) and high (black) quartiles. (D) Cellular components and biological functions of over-represented (black) and under-represented (gray) proteins in PPAT of patients in high quartile, as determined by Gene Ontology enrichment terms. The $-$log10 of the q value are represented on x-axis, and percentage of proteins that were differentially expressed in the pathways are indicated in red on side of each bar plot. (E) Quantification of indicated proteins in PPAT of patients in low and high quartiles ($n = 6$–7 per group) by mass spectrometry. (F) Whole PPAT from patients in low and high groups were stained with anti-YAP1 antibody and phalloidin (to stain actin and facilitate cell visualization) and DAPI (to stain DNA). Panels show merged images. White arrows indicate nuclei of adipocytes. Representative maximum intensity projection of images obtained by 3D confocal microscopy are shown. Scale bars, 50 µm. (G) Quantification of indicated isoforms of tubulin, as in (E) ($n = 6$–7 per group). (H) Whole PPAT from patients in low and high groups were stained with anti-ß-tubulin antibody and DAPI, as in (F). (I) Quantification of indicated proteins, as in (E) ($n = 6$–7 per group). Bars indicate means ± SEM. Statistical differences were calculated using Student's t-test. *$p < 0.05$; **$p < 0.01$; ***$p < 0.001$.

© 2026 The Pathological Society of Great Britain and Ireland. www.pathsoc.org

10969896, 0, Downloaded from https://pathsocjournals.onlinelibrary.wiley.com/doi/10.1002/path.70033 by Ut Southwestern Medical Center, Wiley Online Library on [20/02/2026]. See the Terms and Conditions (https://onlinelibrary.wiley.com/terms-and-conditions) on Wiley Online Library for rules of use; OA articles are governed by the applicable Creative Commons License

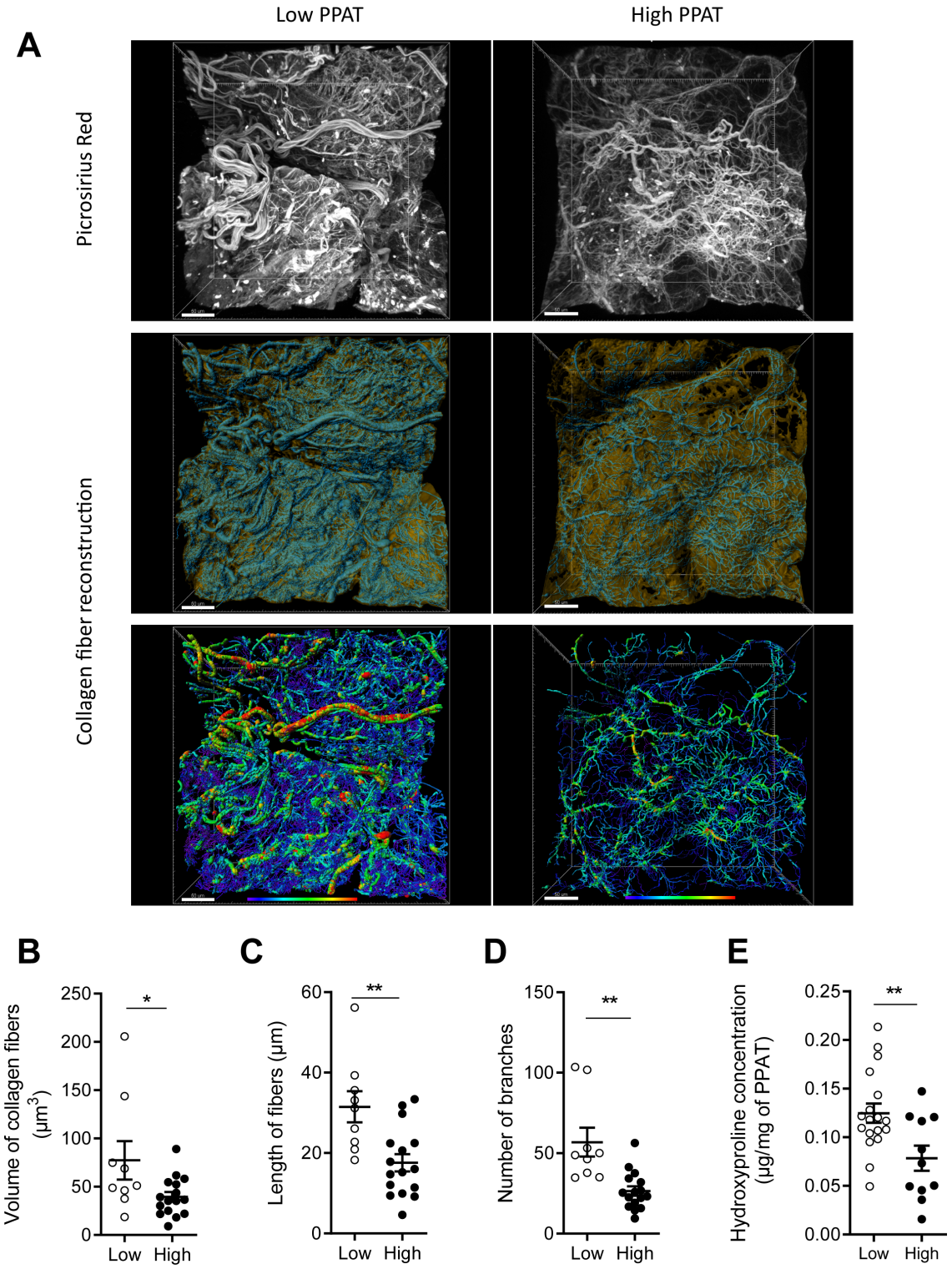

Figure 4. The collagen network in abundant PPAT is relatively loose. (A) Whole PPAT from representative patients in low and high groups were stained with Picrosirius Red to show collagen fibers, imaged in 3D by confocal microscopy (top), reconstructed in 3D (middle), and the reconstructed collagen fiber images were isolated and color-coded according to their diameter (bottom). Scale bars, 50 µm. (B–D) Various morphometric parameters were quantified in 3D images of PPAT from patients in low and high groups after collagen fiber reconstruction (n = 9–16): total collagen volume (B), length of collagen fibers (C), and number of branches per collagen fiber (D). (E) Quantification of hydroxyproline concentration in PPAT from patients in low (n = 18) and high groups (n = 11). Bars indicate means ± SEM. Statistical differences were calculated using Student's t-test. *$p < 0.05$; **$p < 0.0$.

abundance by comparing the residual value of PPAT volume to the linear relationship between PPAT and prostate volume computed from the whole cohort. When we ranked patients into quartiles, we observed no difference in prostate size between groups and patients in the highest quartile had the most aggressive PCa (higher ISUP scores and more high-grade lesions), validating our approach. We then investigated whether

© 2026 The Pathological Society of Great Britain and Ireland. www.pathsoc.org

10969896, 0, Downloaded from https://pathsocjournals.onlinelibrary.wiley.com/doi/10.1002/path.70033 by Ut Southwestern Medical Center, Wiley Online Library on [20/02/2026]. See the Terms and Conditions (https://onlinelibrary.wiley.com/terms-and-conditions) on Wiley Online Library for rules of use; OA articles are governed by the applicable Creative Commons License

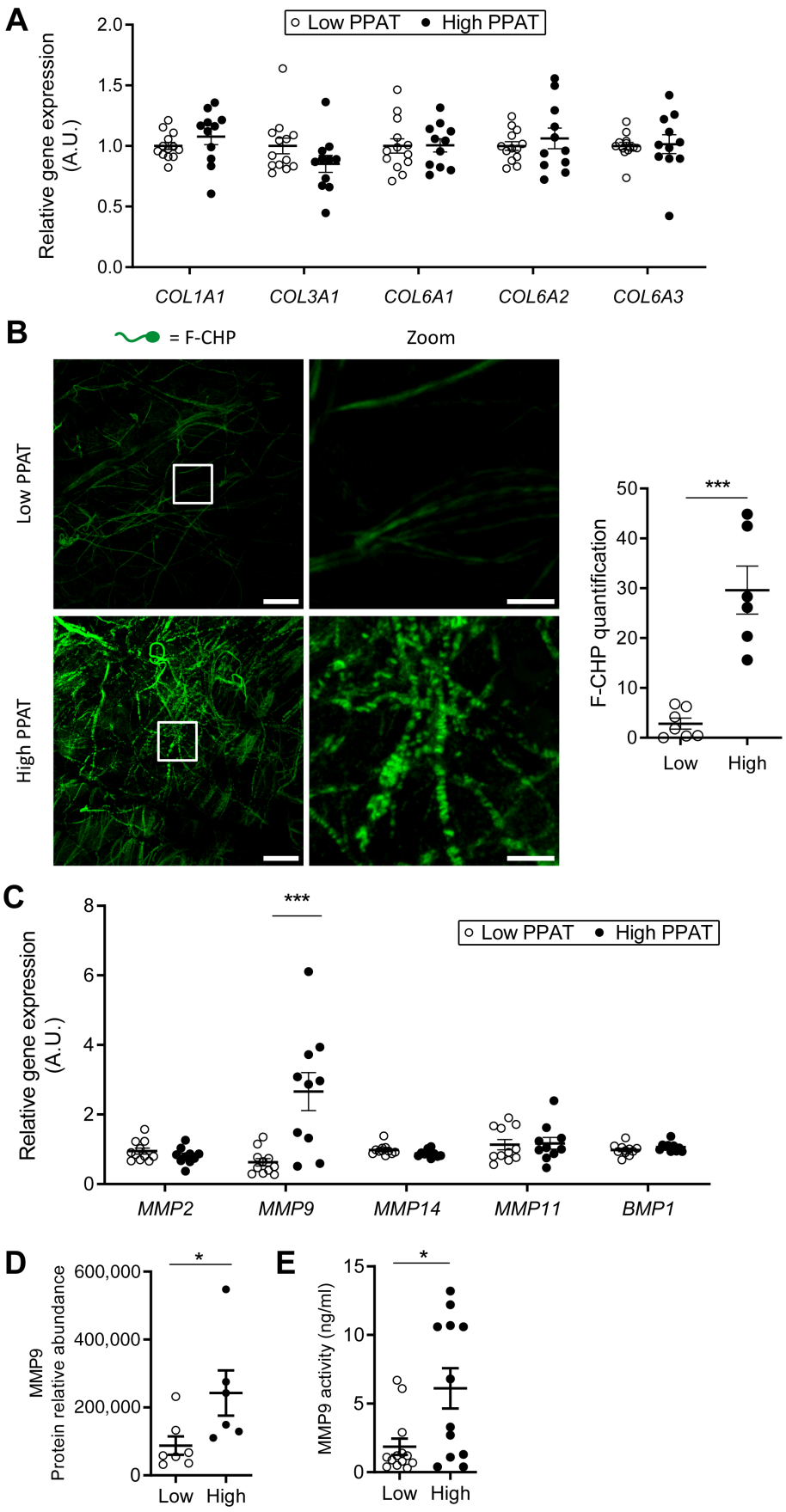

Figure 5 Legend on next page.

10969896, 0, Downloaded from https://pathsocjournals.onlinelibrary.wiley.com/doi/10.1002/path.70033 by Ut Southwestern Medical Center, Wiley Online Library on [20/02/2026]. See the Terms and Conditions (https://onlinelibrary.wiley.com/terms-and-conditions) on Wiley Online Library for rules of use; OA articles are governed by the applicable Creative Commons License

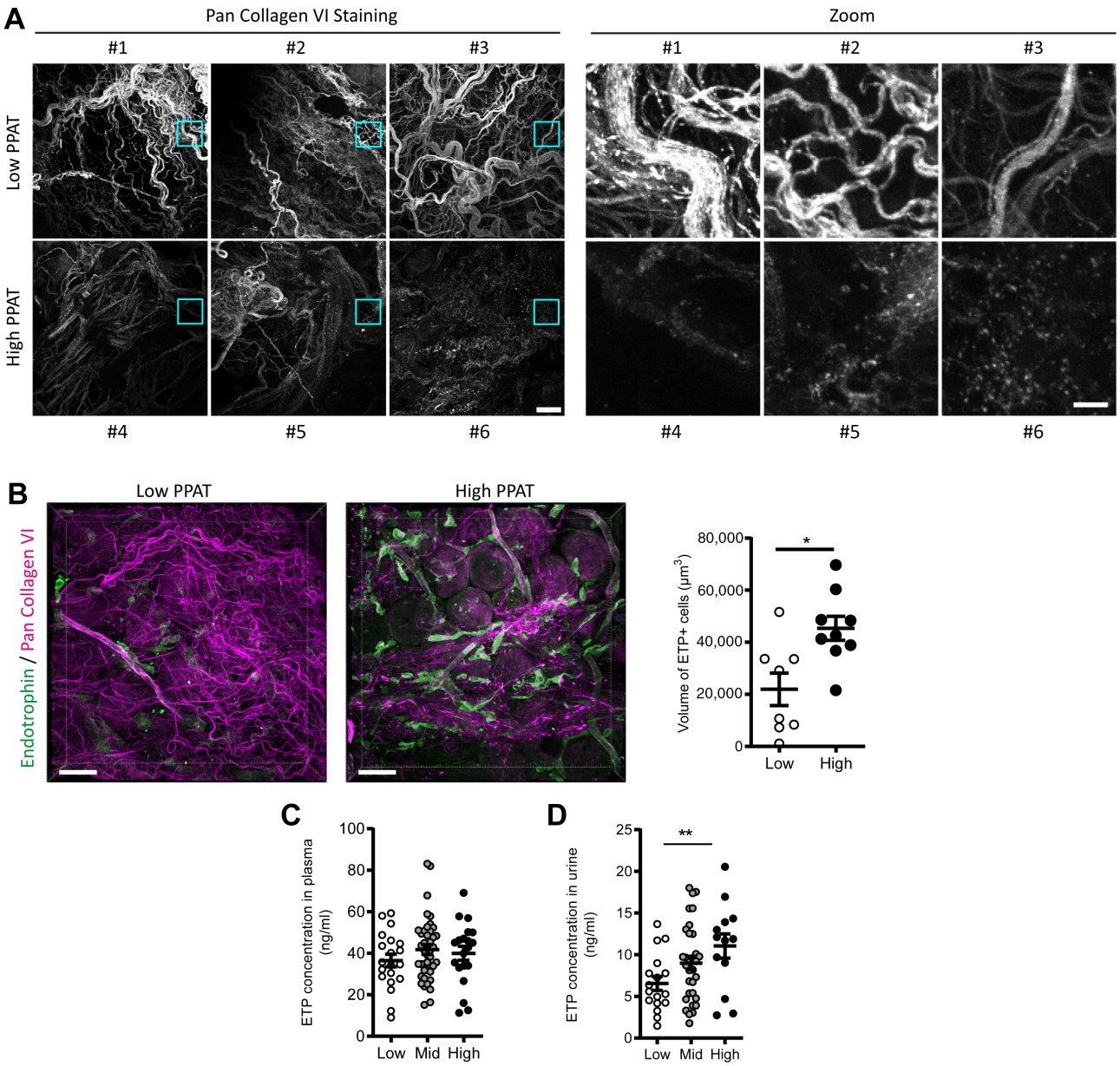

Figure 6. COLVI remodeling is associated with high ETP production in abundant PPAT. (A) Representative confocal images of PPAT from three patients in low quartile (Nos. 1–3) and high quartile (Nos. 4–6) stained with anti-collagen VI antibody that recognizes all collagen VI forms (pan collagen VI). Maximum intensity projections of Z-stacked images at low magnification are shown (left panels) and at higher magnification (Zoom). The areas corresponding to the Zoom images are indicated by the blue lines. Scale bars, 50 µm. (B) Representative confocal immunofluorescence microscopy images of PPAT stained with anti-pan collagen VI (pink) and anti-ETP (green) antibodies. 3D views of Z-stacked images (left). Scale bars, 50 µm. ETP staining was quantified on 3D images (right panel; $n = 8–9$). (C) ETP concentration in plasma from patients with PCa, as quantified by ELISA (low, $n = 20$; mid, $n = 42$; high, $n = 20$). (D) ETP concentration in urine from patients with PCa collected after prostate massage, as quantified by ELISA (low, $n = 17$; mid, $n = 32$; high, $n = 13$). Bars indicate means ± SEM. Statistical differences were calculated using Student's *t*-test (*$p < 0.05$ for B) and ANOVA with post-test for linear trend (**$p < 0.01$ for C and D).

Figure 5. Abundant PPAT exhibits increased collagen degradation likely by MMP9. (A) Relative expression of genes encoding indicated collagen isoforms in whole PPAT from patients in low ($n = 13$) and high groups ($n = 11$). (B) Representative confocal images of PPAT stained with fluorescent collagen-hybridizing peptide (F-CHP). The maximum intensity projection of Z-stacked images (left panel) at low magnification and at higher magnification image (Zoom). The areas corresponding to the Zoom images are indicated by the white squares. Scale bars, 50 µm. F-CHP staining in 3D images was quantified (right panel; $n = 6–7$). (C) Relative expression of genes encoding indicated metalloproteinase (MMP) isoforms in PPAT from patients in low ($n = 11$) and high ($n = 10$) quartiles. (D) Relative MMP9 protein expression quantified in isolated mature adipocytes by mass spectrometry ($n = 6–7$ per quartile). (E) MMP9 enzyme activity in protein extracts of PPAT from patients in low ($n = 13$) and high quartiles ($n = 12$). Bars indicate means ± SEM. Statistical differences were calculated using Student's *t*-test. *$p < 0.05$; ***$p < 0.001$.

© 2026 The Pathological Society of Great Britain and Ireland. www.pathsoc.org

10969896, 0, Downloaded from https://pathsocjournals.onlinelibrary.wiley.com/doi/10.1002/path.70033 by Ut Southwestern Medical Center, Wiley Online Library on [20/02/2026]. See the Terms and Conditions (https://onlinelibrary.wiley.com/terms-and-conditions) on Wiley Online Library for rules of use; OA articles are governed by the applicable Creative Commons License

PPAT characteristics between the different groups differed in their histology, transcriptomes, and proteomes in order to understand how abundant PPATs expand, which was the primary goal of our study.

The most important finding of this study is that abundant PPAT contains a loose meshwork of fibrillar and nonfibrillar collagens, explaining expansion without added inflammation or secretory dysfunction. We previously demonstrated that PPAT exhibited fibrosis preventing its expansion in obese patients, and therefore reshaping the ECM is an essential step for its enlargement [8]. In fact, fibrosis, by generating a mechanical stress on adipocytes, plays a central role in limiting the expandability of AT [31]. A key difference between high- and low-PPAT groups involved COLVI, the most abundant nonfibrillar collagen in AT. In high PPAT, COLVI staining was weak and punctiform and the filament network was disorganized. COLVI interacts with many ECM proteins, including fibronectin and collagen types I, II, and IV, bridging cells to the surrounding connective tissue and organizing the 3D tissue architecture [36]. Thus, the overall loss of collagen may result from initial extensive degradation of COLVI, which probably involves MMP9, which was more abundant in most patients with high PPAT. Degradation of COLVI by MMP9 has been described previously [37], as well as by MMP2 [37], MMP11 [38], and MMP14 [39]. Expression of the latter MMPs and TIMPs was similar in both groups, suggesting that MMP9 is the main enzyme responsible for COLVI degradation in the most abundant PPATs. In addition, this is consistent with a report showing that *in vitro* MMP9 activity, along with MMP2 and MMP16, is key to producing active ETP [40]. We do not yet know what initiates ECM remodeling to allow PPAT expansion. The correlation between the volume of PPAT and the volume of the prostate suggests that steroid hormones might be involved. Consistent with this, MMP9 expression is regulated by androgens [41], and sex hormones influence the metabolism, endocrine functions, and angiogenesis of certain other ATs [42]. This hypothesis deserves further investigation such as comparing PPAT abundance with circulating steroid levels in large clinical cohorts.

This loose collagen network in abundant PPAT will be permissive to adipocyte enlargement, and we observed adipocyte hypertrophy, likely due to increased lipid uptake and decreased lipolysis. PPAT expansion occurs without inflammation or adipocyte dysfunction, and ECM degradation was associated with a decreased expression of proteins involved in mechano-transduction and stiffness sensing. The observed changes in lipid metabolism could be linked to altered mechano-transduction since the two processes have been found to be interconnected [43]. This expansion in a context of decreased mechanical constraints led to a 'stress-free' expansion, allowing the adipocytes to enlarge without cell death, which prevents accumulation of macrophages and, subsequently, the occurrence of an inflammatory microenvironment. Evidence from mouse models deficient in ECM (lack of COLVI) [44] or overexpressing ECM remodeling proteins (MMP14) [39] supports our interpretation. In both cases, the decrease in the ECM stiffness of AT, which released the mechanical stress, led to healthy AT expansion upon exposure to a high-fat diet [44]. Taken together, our results demonstrate that PPAT expands by a unique mechanism that protects it from further dysfunction.

Extensive ECM remodeling in abundant PPAT results in features known to favor PCa and other prostate disorders. ECM binds growth factors and cytokines released during remodeling, which can act on nearby normal and PCa cells [45]. ECM also interacts directly with epithelial cells through integrins, regulating adhesion, proliferation, or survival [45]. Among ECM-derived components, ETP, a COLVI fragment, was highly expressed in abundant PPAT. Adipocyte-derived ETP favors breast tumor progression and resistance to therapy in genetically engineered mice [46] and in xenografted human tumors [21]. Finally, collagen degradation may also serve as a nutrient source through proline release [47]. Deciphering these mechanisms requires a model capable of reproducing the interaction between abundant PPAT and normal or tumoral epithelial cells. While explant culture leads to rapid dedifferentiation [48], alternatives like the 'sandwiched AT' model [49] could provide more stable experimental systems.

In conclusion, we have deciphered for the first time the original mechanism that allows human PPAT to expand and demonstrated that it relies on ECM reshaping that is, to our knowledge, a unique mechanism of expansion among adipose depots. This work opens new avenues to decipher the role of abundant PPAT in PCa at both fundamental and clinical levels.

Acknowledgements

This work benefited from the Toulouse Réseau Imagerie (TRI)-RIO optical imaging platform at the Institute of Pharmacology and Structural Biology (Genotoul, Toulouse, France). We acknowledge Life Science Editors for professional scientific editing during the preparation of the manuscript. This study was supported by the Ligue Nationale Contre le Cancer (Équipe Labélisée), the French National Cancer Institute (INCA PL-BIO 2016-176 to AB, BM, PV and CM), by the Fondation Toulouse Cancer Santé (to AB, BM, OBS, PV and CM) and by the Fondation ARC (Association de Recherche contre le Cancer) Programmes Labelisés 2016 (to AB, PV and CM). The work was also funded in part by the Infrastructures Nationales en Biologie et Santé (INBS) (ProFI, Proteomics French Infrastructure project, ANR-10-INBS-08) (to OBS). DE received a postdoctoral fellowship from the Fondation pour La Recherche Médicale (SPF201809007124).

Author contributions statement

DE and AT conducted and analyzed most of the experiments presented in the manuscript and prepared the

© 2026 The Pathological Society of Great Britain and Ireland. www.pathsoc.org

10969896, 0, Downloaded from https://pathsocjournals.onlinelibrary.wiley.com/doi/10.1002/path.70033 by Ut Southwestern Medical Center, Wiley Online Library on [20/02/2026]. See the Terms and Conditions (https://onlinelibrary.wiley.com/terms-and-conditions) on Wiley Online Library for rules of use; OA articles are governed by the applicable Creative Commons License

figures. AT, MR and DM performed the segmentations and measurements of PPAT and prostate volumes. DE developed the statistic model defining the PPAT abundance. CF performed the H&E staining of PPAT samples and AT performed the adipocyte size measurement. AT performed the flow cytometry experiments with the help of CB under the supervision of AB. AT and MH performed the ELISA experiments with the help of SLG under the supervision of PV. DE and MDP performed the proteomic experiments and the analysis of the proteomic data under the supervision of OBS. CH and YJ performed the qPCR experiments and MMP9 activity measurement. DE and ML performed the microscopy experiments with the help of SP, NVA and SD. DB performed the endotrophin dosage in human fluids under the supervision of PES. ML helped to write the manuscript and to prepare the figures. BM, CM, ND, MT, MR harvested the human periprostatic tissue and fluids samples and CM and MR collected the clinical data. MM participated to tissue processing. DE, DM and Catherine Muller (CM) supervised the study and wrote the manuscript. All the authors reviewed the manuscript. All the authors agreed with the final version of the manuscript.

Data availability statement

The mass spectrometry proteomics data have been deposited at the ProteomeXchange Consortium via the PRIDE partner repository with the dataset identifier PXD038514 (https://www.ebi.ac.uk/pride/archive/projects/PXD038514).

References

1. Ishidoya S, Endoh M, Nakagawa H, *et al*. Novel anatomical findings of the prostatic gland and the surrounding capsular structures in the normal prostate. *Tohoku J Exp Med* 2007; **212:** 55–62.
2. Rosen ED, Spiegelman BM. What we talk about when we talk about fat. *Cell* 2014; **156:** 20–44.
3. Kahn CR, Wang G, Lee KY. Altered adipose tissue and adipocyte function in the pathogenesis of metabolic syndrome. *J Clin Invest* 2019; **129:** 3990–4000.
4. Zwick RK, Guerrero-Juarez CF, Horsley V, *et al*. Anatomical, physiological, and functional diversity of adipose tissue. *Cell Metab* 2018; **27:** 68–83.
5. Estève D, Roumiguié M, Manceau C, *et al*. Periprostatic adipose tissue: a heavy player in prostate cancer progression. *Curr Opin Endocr Metab Res* 2020; **10:** 29–35.
6. Nassar ZD, Aref AT, Miladinovic D, *et al*. Peri-prostatic adipose tissue: the metabolic microenvironment of prostate cancer. *BJU Int* 2018; **121:** 9–21.
7. Passos GR, Ghezzi AC, Antunes E, *et al*. The role of periprostatic adipose tissue on prostate function in vascular-related disorders. *Front Pharmacol* 2021; **12:** 626155.
8. Roumiguié M, Estève D, Manceau C, *et al*. Periprostatic adipose tissue displays a chronic hypoxic state that limits its expandability. *Am J Pathol* 2022; **192:** 926–942.
9. Miladinovic D, Cusick T, Mahon KL, *et al*. Assessment of periprostatic and subcutaneous adipose tissue lipolysis and adipocyte size from men with localized prostate cancer. *Cancer* 2020; **12:** 1385.
10. Woo S, Cho JY, Kim SY, *et al*. Periprostatic fat thickness on MRI: correlation with Gleason score in prostate cancer. *AJR Am J Roentgenol* 2015; **204:** W43–W47.
11. Zhang Q, Sun L, Qi J, *et al*. Periprostatic adiposity measured on magnetic resonance imaging correlates with prostate cancer aggressiveness. *Urol J* 2014; **11:** 1793–1799.
12. Zhai T-S, Hu L-T, Ma W-G, *et al*. Peri-prostatic adipose tissue measurements using MRI predict prostate cancer aggressiveness in men undergoing radical prostatectomy. *J Endocrinol Investig* 2021; **44:** 287–296.
13. van Roermund JGH, Hinnen KA, Tolman CJ, *et al*. Periprostatic fat correlates with tumour aggressiveness in prostate cancer patients. *BJU Int* 2011; **107:** 1775–1779.
14. Liu B-H, Mao Y-H, Li X-Y, *et al*. Measurements of peri-prostatic adipose tissue by MRI predict bone metastasis in patients with newly diagnosed prostate cancer. *Front Oncol* 2024; **14:** 1393650.
15. Xiong T, Cao F, Zhu G, *et al*. MRI-measured periprostatic adipose tissue volume as a prognostic predictor in prostate cancer patients undergoing laparoscopic radical prostatectomy. *Adipocyte* 2023; **12:** 2201964.
16. Jiang S, Li Y, Guo Y, *et al*. MRI-measured periprostatic to subcutaneous adipose tissue thickness ratio as an independent risk factor in prostate cancer patients undergoing radical prostatectomy. *Sci Rep* 2024; **14:** 20896.
17. Dahran N, Szewczyk-Bieda M, Wei C, *et al*. Normalized periprostatic fat MRI measurements can predict prostate cancer aggressiveness in men undergoing radical prostatectomy for clinically localised disease. *Sci Rep* 2017; **7:** 4630.
18. Tan WP, Lin C, Chen M, *et al*. Periprostatic fat: a risk factor for prostate cancer? *Urology* 2016; **98:** 107–112.
19. Henriksen K, Genovese F, Reese-Petersen A, *et al*. Endotrophin, a key marker and driver for fibroinflammatory disease. *Endocr Rev* 2024; **45:** 361–378.
20. Estève D, Boulet N, Belles C, *et al*. Lobular architecture of human adipose tissue defines the niche and fate of progenitor cells. *Nat Commun* 2019; **10:** 2549.
21. Bu D, Crewe C, Kusminski CM, *et al*. Human endotrophin as a driver of malignant tumor growth. *JCI Insight* 2019; **5:** 125094.
22. Bouyssié D, Hesse A-M, Mouton-Barbosa E, *et al*. Proline: an efficient and user-friendly software suite for large-scale proteomics. *Bioinformatics* 2020; **36:** 3148–3155.
23. Camhi SM, Bray GA, Bouchard C, *et al*. The relationship of waist circumference and BMI to visceral, subcutaneous, and total body fat: sex and race differences. *Obesity (Silver Spring)* 2011; **19:** 402–408.
24. Costello AJ. Considering the role of radical prostatectomy in 21st century prostate cancer care. *Nat Rev Urol* 2020; **17:** 177–188.
25. Pellegrinelli V, Carobbio S, Vidal-Puig A. Adipose tissue plasticity: how fat depots respond differently to pathophysiological cues. *Diabetologia* 2016; **59:** 1075–1088.
26. Ouchi N, Parker JL, Lugus JJ, *et al*. Adipokines in inflammation and metabolic disease. *Nat Rev Immunol* 2011; **11:** 85–97.
27. Dupont S, Morsut L, Aragona M, *et al*. Role of YAP/TAZ in mechanotransduction. *Nature* 2011; **474:** 179–183.
28. Ma B, Cheng H, Gao R, *et al*. Zyxin-Siah2-Lats2 axis mediates cooperation between hippo and TGF-β signalling pathways. *Nat Commun* 2016; **7:** 11123.
29. Rausch V, Hansen CG. The hippo pathway, YAP/TAZ, and the plasma membrane. *Trends Cell Biol* 2020; **30:** 32–48.
30. Ichikawa T, Kita M, Matsui TS, *et al*. Vinexin family (SORBS) proteins play different roles in stiffness-sensing and contractile force generation. *J Cell Sci* 2017; **130:** 3517–3531.
31. Sun K, Tordjman J, Clément K, *et al*. Fibrosis and adipose tissue dysfunction. *Cell Metab* 2013; **18:** 470–477.
32. Hwang J, Huang Y, Burwell TJ, *et al*. In situ imaging of tissue remodeling with collagen hybridizing peptides. *ACS Nano* 2017; **11:** 9825–9835.
33. Sun K, Park J, Gupta OT, *et al*. Endotrophin triggers adipose tissue fibrosis and metabolic dysfunction. *Nat Commun* 2014; **5:** 3485.

© 2026 The Pathological Society of Great Britain and Ireland. www.pathsoc.org

10969896, 0, Downloaded from https://pathsocjournals.onlinelibrary.wiley.com/doi/10.1002/path.70033 by Ut Southwestern Medical Center, Wiley Online Library on [20/02/2026]. See the Terms and Conditions (https://onlinelibrary.wiley.com/terms-and-conditions) on Wiley Online Library for rules of use; OA articles are governed by the applicable Creative Commons License

34. Fujita K, Nonomura N. Urinary biomarkers of prostate cancer. *Int J Urol* 2018; **25:** 770–779.
35. Loeb S, Kettermann A, Carter HB, *et al*. Prostate volume changes over time: results from the Baltimore longitudinal study of aging. *J Urol* 2009; **182:** 1458–1462.
36. Cescon M, Gattazzo F, Chen P, *et al*. Collagen VI at a glance. *J Cell Sci* 2015; **128:** 3525–3531.
37. Veidal SS, Karsdal MA, Vassiliadis E, *et al*. MMP mediated degradation of type VI collagen is highly associated with liver fibrosis—identification and validation of a novel biochemical marker assay. *PLoS One* 2011; **6:** e24753.
38. Motrescu ER, Blaise S, Etique N, *et al*. Matrix metalloproteinase-11/stromelysin-3 exhibits collagenolytic function against collagen VI under normal and malignant conditions. *Oncogene* 2008; **27:** 6347–6355.
39. Li X, Zhao Y, Chen C, *et al*. Critical role of matrix metalloproteinase 14 in adipose tissue remodeling during obesity. *Mol Cell Biol* 2020; **40:** e00519–e00564.
40. Jo W, Kim M, Oh J, *et al*. MicroRNA-29 ameliorates fibro-inflammation and insulin resistance in HIF1α-deficient obese adipose tissue by inhibiting Endotrophin generation. *Diabetes* 2022; **71:** 1746–1762.
41. Tang Q, Cheng B, Dai R, *et al*. The role of androgen receptor in cross talk between stromal cells and prostate cancer epithelial cells. *Front Cell Dev Biol* 2021; **9:** 729498.
42. Karastergiou K, Smith SR, Greenberg AS, *et al*. Sex differences in human adipose tissues—the biology of pear shape. *Biol Sex Differ* 2012; **3:** 13.
43. de Luca M, Mandala M, Rose G. Towards an understanding of the mechanoreciprocity process in adipocytes and its perturbation with aging. *Mech Ageing Dev* 2021; **197:** 111522.
44. Khan T, Muise ES, Iyengar P, *et al*. Metabolic dysregulation and adipose tissue fibrosis: role of collagen VI. *Mol Cell Biol* 2009; **29:** 1575–1591.
45. Bonnans C, Chou J, Werb Z. Remodelling the extracellular matrix in development and disease. *Nat Rev Mol Cell Biol* 2014; **15:** 786–801.
46. Park J, Scherer PE. Adipocyte-derived endotrophin promotes malignant tumor progression. *J Clin Invest* 2012; **122:** 4243–4256.
47. Olivares O, Mayers JR, Gouirand V, *et al*. Collagen-derived proline promotes pancreatic ductal adenocarcinoma cell survival under nutrient limited conditions. *Nat Commun* 2017; **8:** 16031.
48. Dufau J, Shen JX, Couchet M, *et al*. In vitro and ex vivo models of adipocytes. *Am J Phys Cell Phys* 2021; **320:** C822–C841.
49. Fontenot JJ, Lau FH. In vitro culture of white adipose tissue. *Methods Mol Biol* 2024; **2783:** 279–285.

SUPPLEMENTARY MATERIAL ONLINE

Supplementary materials and methods

Figure S1. Subcutaneous and perirectal AT areas are correlated with BMI

Figure S2. NPFV is not an appropriate measure of PPAT abundance

Figure S3. Abundant PPAT is associated with aggressive PCa

Figure S4. Adipose progenitor cell and lymphocyte subsets are not modified according to PPAT abundance

Figure S5. Proteins involved in lipolysis and lipid uptake are underrepresented and overrepresented in abundant PPAT

Figure S6. Absence of modifications of LOX or TIMP isoforms expression in low versus abundant PPAT

Table S1. Anthropometric characteristics of PCa patients

Table S2. Clinical and pathological characteristics of PCa patients

Table S3. Antibodies used for flow cytometry

Table S4. Primers used for RT-qPCR

Table S5. Antibodies used for microscopy

Table S6. Clinical and pathological characteristics of PCa patients according to PPAT

Table S7. Anthropometric characteristics of patients in cohort used for endotrophin quantification in biological fluids

Table S8. Clinical and pathological characteristics of patients in cohort used for endotrophin quantification in biological fluid

Table S9. Protein abundances in low- and high-PPAT samples from proteomic analysis.

Table S10. Top 10 under- and over-represented proteins identified by spectrometry-based proteomic in high PPAT relative to low PPAT

© 2026 The Pathological Society of Great Britain and Ireland. www.pathsoc.org

10969896, 0, Downloaded from https://pathsocjournals.onlinelibrary.wiley.com/doi/10.1002/path.70033 by Ut Southwestern Medical Center, Wiley Online Library on [20/02/2026]. See the Terms and Conditions (https://onlinelibrary.wiley.com/terms-and-conditions) on Wiley Online Library for rules of use; OA articles are governed by the applicable Creative Commons License